



# Invariant scaling of impulsively started polygonal disks

Dylan Caverly<sup>1</sup>  and Jovan Nedić<sup>1</sup> 

<sup>1</sup>Department of Mechanical Engineering, McGill University, Montréal, QC H3A 0C3, Canada

Corresponding author: Dylan Caverly, [dylan.caverly@mail.mcgill.ca](mailto:dylan.caverly@mail.mcgill.ca)

(Received 28 October 2024; revised 4 March 2025; accepted 6 March 2025)

---

The flow behind impulsively started circular and polygonal plates is investigated experimentally, using particle image velocimetry at several azimuthal angles. Observing plates accelerating up to a steady Reynolds number  $Re = 27\,000$ , the three invariants of the motion, circulation  $\Gamma$ , hydrodynamic impulse  $I$  and kinetic energy  $E$ , were scaled against four candidate lengths: the hydraulic diameter, perimeter, circumscribed diameter and the square root of the area. Of these, the square root of the area was found to best collapse all the data. Investigating the three-dimensionality of the flow, it is found that, while a single-plane measurement can provide a reasonable approximation for  $\Gamma$  behind plates, multiple planes are necessary to accurately estimate  $E$  and  $I$ .

**Key words:** vortex dynamics

---

## 1. Introduction

The dynamics of coherent structures around impulsive and steady flat plates are of particular interest in aero- and hydrodynamic applications, primarily due to their major contribution to the drag force generated by the body. For flat plates in a steady flow, studies have focused primarily on the formation and dynamics of a vortex loop to explore possible drag reduction mechanisms (Fernando & Rival 2016a). Impulsively started plates are typically used to model biological phenomena, such as flapping wings or fins (Pullin & Wang 2004; Green & Smits 2008; Beckwith & Babinsky 2009), with the plate accelerated quickly from rest, and maintained at a desired velocity. To compare the flow properties around plates of different geometries, universal scaling factors are necessary. Typically, flow properties such as forces and circulation require scaling factors for velocity and length. It is accepted that the characteristic velocity should be the steady-state velocity  $U$ ; however, the most appropriate characteristic length is still an open question.

The natural characteristic length for circular plates is the plate diameter  $D$ , and has successfully scaled vortex ring formation in its wake (Yang, Jia & Lin 2012; Xiang *et al.* 2021), the drag coefficient (Li *et al.* 2022) and shear layer properties (Rosi & Rival 2017). For impulsively started disks, added mass plays a significant role in the generation of drag force, and hence in the circulation of the flow field and other flow invariants. One could therefore argue that an appropriate characteristic length should include the area of the plate, since the mass displaced by the plate would be directly proportional to its area and the length that the plate is surged. One possible, and often used, length scale that accounts for the area is the hydraulic diameter: the ratio of a plate's area to one-quarter of its perimeter,  $D_h = 4A/P$  (Fernando & Rival 2016a,b; Fernando, Weymouth & Rival 2020; Reijtenbagh, Tummers & Westerweel 2023). For regular polygons,  $D_h$  is equal to a shape's inscribed diameter; for example, the hydraulic diameter of a circle is its diameter, while  $D_h$  of a square is one side length. Studying circular, elliptical, square and rectangular plates, Fernando & Rival (2016b) argued that the hydraulic diameter is an appropriate characteristic length to scale forces and circulation, as it considers both the area and perimeter of the plate. The argument often given is that the area sets the mass to be displaced, whereas the perimeter accounts for how the mass is displaced in space. While peak forces on plates were similar for square and circular plates with equivalent hydraulic diameters, transient forces were not. Fernando & Rival (2016b) also demonstrated that for constant hydraulic diameter plates, increasing the aspect ratio resulted in lower peak forces and earlier vortex pinch-off. Reijtenbagh *et al.* (2023) used a 'natural length' as a characteristic length to predict peak forces on accelerating plates. For the three-dimensional thin-plate geometries tested, this characteristic length is equivalent to the hydraulic diameter of a square or circle, or the shorter length of a rectangular plate. They found that the square root of the non-dimensional acceleration rate was necessary to model the transient forces on the accelerating plates. The authors noted that a minor adjustment to the drag coefficient was necessary to scale the peak forces; simply relying on the natural length and acceleration was insufficient, and an additional scaling factor based on plate geometry was required.

In contrast, Kaiser, Kriegseis & Rival (2020), who investigated impulsively started circular disks with sinusoidal perturbations on their perimeter, used the mean diameter of the plate as a characteristic length. This dimension is similar to, but slightly different (within 1 %) from, that Higuchi, Anderson & Zhang (1996) used, namely the equivalent diameter  $D_{eq}$  (the diameter of a circle with an equal area) in their flow visualisation study of polygonal plates. Although only the vortex kinematics were investigated, it demonstrated that such a scaling could work for impulsively generated flows. These results also showed that the vortex structure resembles the shape of the plate at early times. This scaling, which is equivalent to the square root of the area,  $\ell = \sqrt{A}$ , has also been used for plates undergoing steady-state motion (Fail, Lawford & Eyre 1959; Nedić, Ganapathisubramani & Vassilicos 2013a; Kubota & Endo 2022). Of particular note is that  $\ell$  produced self-similar scalings of turbulent axisymmetric wakes, generated by non-axisymmetric plates, including squares and fractal plates (Nedić, Vassilicos & Ganapathisubramani 2013b). This would suggest that the perimeter might not be required for scaling purposes.

In the vast majority of previous studies, only the circulation of the flow field, as well as the drag force, have been investigated and scaled with the hydraulic diameter. Of the remaining two invariants, those being the hydraulic impulse and kinetic energy, only the kinetic energy for a disk has been investigated (de Guyon & Mulleners 2022). As all three invariants are based on the same flow field properties, the ideal characteristic length must

collapse all three invariants. Given the success of  $\ell = \sqrt{A}$  as a scaling parameter for steady wakes, its effectiveness for impulsive flows is worth exploring. This length scale is further justified by its relation to the plate area, which in turn has been shown to scale added mass effects. Our primary objective, therefore, is to ascertain how well  $\ell = \sqrt{A}$  collapses all three invariants of the flow, as compared with the hydraulic diameter. A selection of other possible characteristic lengths is also considered for comparison.

A secondary objective is to determine how accurately the invariants can be estimated from a finite number of measurement planes. Higuchi *et al.* (1996) demonstrated that the vortex formed on an impulsively started polygon plate follows the shape of the plate in early times. Therefore, it stands to reason that multiple planes must be used to accurately determine all the invariants, and hence test the validity of the proposed characteristic length scaling. This objective is further motivated by the works of Fernando & Rival (2016b) who mentioned that such measurements would be of interest.

## 2. Characteristic lengths

For a regular polygon, four candidate length scales can be defined: the square root of area  $\ell = \sqrt{A}$ , the hydraulic diameter  $D_h$ , the circumscribed diameter  $D_o$  and the perimeter  $P$ . Definitions, and justification, for the first two were presented earlier, hence we address the latter two here. Studying vortex loop formation behind square plates, Fernando & Rival (2016b) noted that the vortex ring had a radius  $R_c$  that lay between the inscribed and circumscribed radii,  $D_h/2 \leq R_c \leq \sqrt{2}D_h/2$ . de Guyon & Mulleners (2021) demonstrated that the circulation of the vortex ring behind conical shapes is best scaled with the vortex ring diameter. Since the vortex ring radius scales approximately with circumscribed radii, we will also consider this length in our scaling analysis. Finally, as  $D_h$  considers both the area and perimeter, we shall also consider the perimeter as a potential length scale, which can be viewed as a scale of the total circumference of the vortex loop. Remaining consistent with the denominator of hydraulic diameter, we use  $P/4$  as a potential scale. For a square plate, this value is identical to the hydraulic diameter and the square root of the area. Increasing the perimeter of a plate increases the perimeter of the shear layer, which should lead to more entrained fluid, and, as shown by Kaiser *et al.* (2020), can lead to enhanced entrainment into the vortex core.

## 3. Experimental set-up and methodology

### 3.1. Choice of regular polygon plates

Five plates are considered in this study, including a circle and four low-order regular polygonal geometries: hexagon, pentagon, square and triangle. In the limit of infinite sides, that is to say a circle,  $D_o/\ell$  and  $D_h/\ell$  both tend to  $2\pi^{-0.5}$ , while  $P/4\ell$  tends to  $\sqrt{\pi}/2$ . Both the circumscribed diameter and the perimeter decrease as the number of sides of a regular polygon increases (for a constant area), while the hydraulic diameter increases. For a square plate, which is the most common polygon plate used in the literature,  $\ell = D_h = P/4$ , and the difference with a circle is  $\approx 13\%$ . By exploring a wider range of polygons, specifically the triangle plate, the difference in  $D_h$  and  $P/4$  compared with a circle increases to  $\approx 27\%$ , while for  $D_o$  the difference is  $\approx 56\%$ .

### 3.2. Apparatus

Experiments were performed in an octagonal acrylic tank with an inscribed diameter of 215 mm and 6 mm thick walls, filled with water to a height of 400 mm. A rendering of

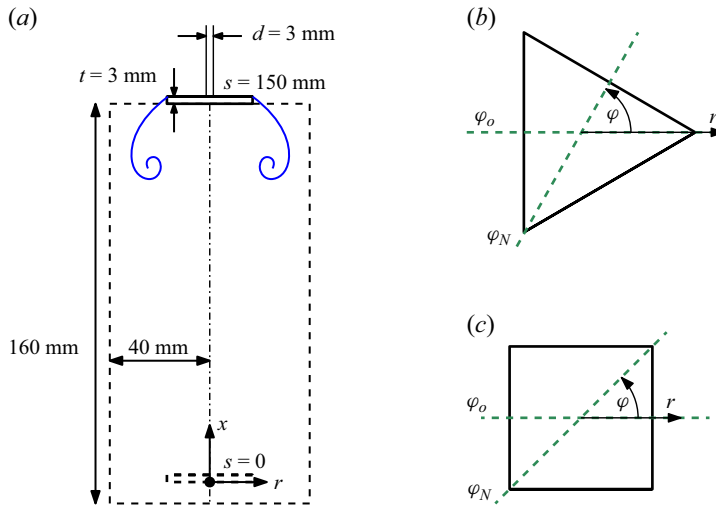


Figure 1. Rendering of the experimental set-up: (a) side view of experiment, (b) top view for a triangular plate, (c) top view of a square plate.

Shape	$\sqrt{A}$ (mm)	$D_h$ (mm)	$D_o$ (mm)	$P/4$ (mm)
Circle	35.4	39.9	39.9	31.3
Hexagon	35.4	38.0	43.9	32.9
Pentagon	35.4	37.1	45.9	33.7
Square	35.4	35.4	50.0	35.4
Triangle	35.4	31.1	62.0	40.3

Table 1. Candidate length scales for each plate.

the set-up is provided in figure 1. A flat acrylic plate is pulled by an electric actuator (a modified version of the Ultramotion ServoCylinder A2 – see Limbourg & Nedić 2021). The actuator has a maximum range of motion of 320 mm and a maximum speed of  $800 \text{ mm s}^{-1}$ . The water temperature was measured regularly during the measurements and was found to be between  $19^\circ\text{C}$  and  $21^\circ\text{C}$ , corresponding to a kinematic viscosity ranging from  $0.98 \text{ mm}^2 \text{ s}^{-1}$  to  $1.03 \text{ mm}^2 \text{ s}^{-1}$ . For simplicity, the kinematic viscosity of water is assumed to be  $1.0 \text{ mm}^2 \text{ s}^{-1}$  when computing Reynolds numbers.

Each plate was pulled by the actuator from rest at a constant acceleration of  $a = 12.5 \text{ m}^{-1} \text{ s}^2$ , until it achieved, and subsequently maintained, a constant velocity of  $U = 0.750 \text{ ms}^{-1}$ . All plates had an area of  $A = 1250 \text{ mm}^2$  and a thickness of 3 mm. This plate area corresponds to a blockage ratio of approximately 3.3 %, well below acceptable blockage limits. Using the square root of the area  $\ell = \sqrt{A}$  as a characteristic length, the corresponding Reynolds numbers was  $Re = 27\,000$ . The non-dimensional acceleration  $a^* = a\ell/U^2 = 0.785$ . Plate properties are presented in table 1, showing all candidate length scales for each plate.

### 3.3. Particle image velocimetry

Time-resolved planar particle image velocimetry (PIV) was used to measure the velocity field in the wake of the plates. A cylindrical  $r-\varphi-x$  coordinate system is used, where the

plate travels in the  $x$ -direction. A continuous 5 W, 532 nm laser, along with a Powell lens and various optics, was used to create a 1.5mm thick vertical laser sheet in the  $r-x$  plane of the flow field, passing through the centre of the plate, at a specific azimuthal angle  $\varphi$ . The flow was seeded with 20  $\mu\text{m}$  polyamide particles (specific density of 1.03), with an average of seven particles per final interrogation window.

The high-speed camera (Photron FASTCAM Mini WX50) was placed to capture a region of approximately  $(r, x) \in [-40, 40] \text{ mm} \times [-10, 150] \text{ mm}$ , where  $(0, 0)$  is the centre of the plate at rest. The high-speed camera has a resolution of  $1024 \times 2048$  pixels at the operating frame-rate of  $1500 \text{ s}^{-1}$ . A three-pass cross-correlation algorithm is used, ending in a  $24 \times 24$  pixel interrogation window, with 50% overlap. This results in a  $86 \times 171$  vector field with data spacing of  $\Delta r = \Delta z = 0.91 \text{ mm}$  and spatial resolution of 1.88 mm.

### 3.3.1. Selection of planes

To observe the non-axisymmetric aspects of the vortex loop formation, measurements were taken in  $r-z$  planes at several azimuthal angles, in  $5^\circ$  increments. The selection of which planes to observe was based on the dihedral group  $D_n$  of the plate geometry. Figure 1 provides the reference coordinate system for  $n$ -sided polygons, including the first and last planes measured,  $\varphi_o$  and  $\varphi_N$ , respectively. For odd  $n$ ,  $\varphi_o$  was defined as an axis of symmetry, which crosses through one vertex and the midpoint of the opposite side. For even  $n$ ,  $\varphi_o$  was defined as a midline axis of symmetry, connecting opposite midpoints of edges. Due to the assumed  $D_n$  symmetry of the flow, measurements were required only in the range between two sets of reflection axes. For example, in the case of the square plate, this involved azimuthal angles  $\varphi \in [0^\circ, 45^\circ]$ , which also captured the range of  $\varphi \in [180^\circ, 225^\circ]$ . This information was reflected and repeated to assume  $D_n$  symmetry, to observe the full  $360^\circ$  of the flow field. In the case of the circular disk, three azimuthal angles were selected in  $15^\circ$  increments. Measurements at each angle  $\varphi$  were repeated five times for each plate. For all calculations, only measurements behind the plate are considered. In subsection 4.3, we will further address how the number of measurement planes affects the results, and determine the minimum number of planes to accurately characterise the flow.

### 3.4. Invariants of the flow

For an unbounded axisymmetric flow with no swirl, the principal invariants of the motion are the circulation, the hydrodynamic impulse and the kinetic energy:

$$\Gamma = \iint \omega dr dx, \quad I = \pi \rho \iint \omega r^2 dr dx, \quad E = \pi \rho \iint (u_r^2 + u_x^2) dr dx, \quad (3.1a-c)$$

where  $\omega$  is the vorticity of the flow,  $\rho$  is the density of the fluid, and  $u_r, u_x$  are the velocity components in the  $r$ - and  $x$ - directions, respectively. Although we do not expect the flow to be axisymmetric, again referring to the observations of Higuchi *et al.* (1996), these three properties will remain invariants of the flow under the condition that the integral is taken about the axis of dihedral symmetry. For such a condition, circulation, kinetic energy and hydrodynamic impulse (3.1) becomes:

$$\Gamma = \frac{1}{2\pi} \iiint \omega dr dx d\varphi, \quad I = \frac{1}{2} \rho \iiint \omega r^2 dr dx d\varphi, \quad E = \frac{1}{2} \rho \iiint (u_r^2 + u_x^2) dr dx d\varphi. \quad (3.2a-c)$$

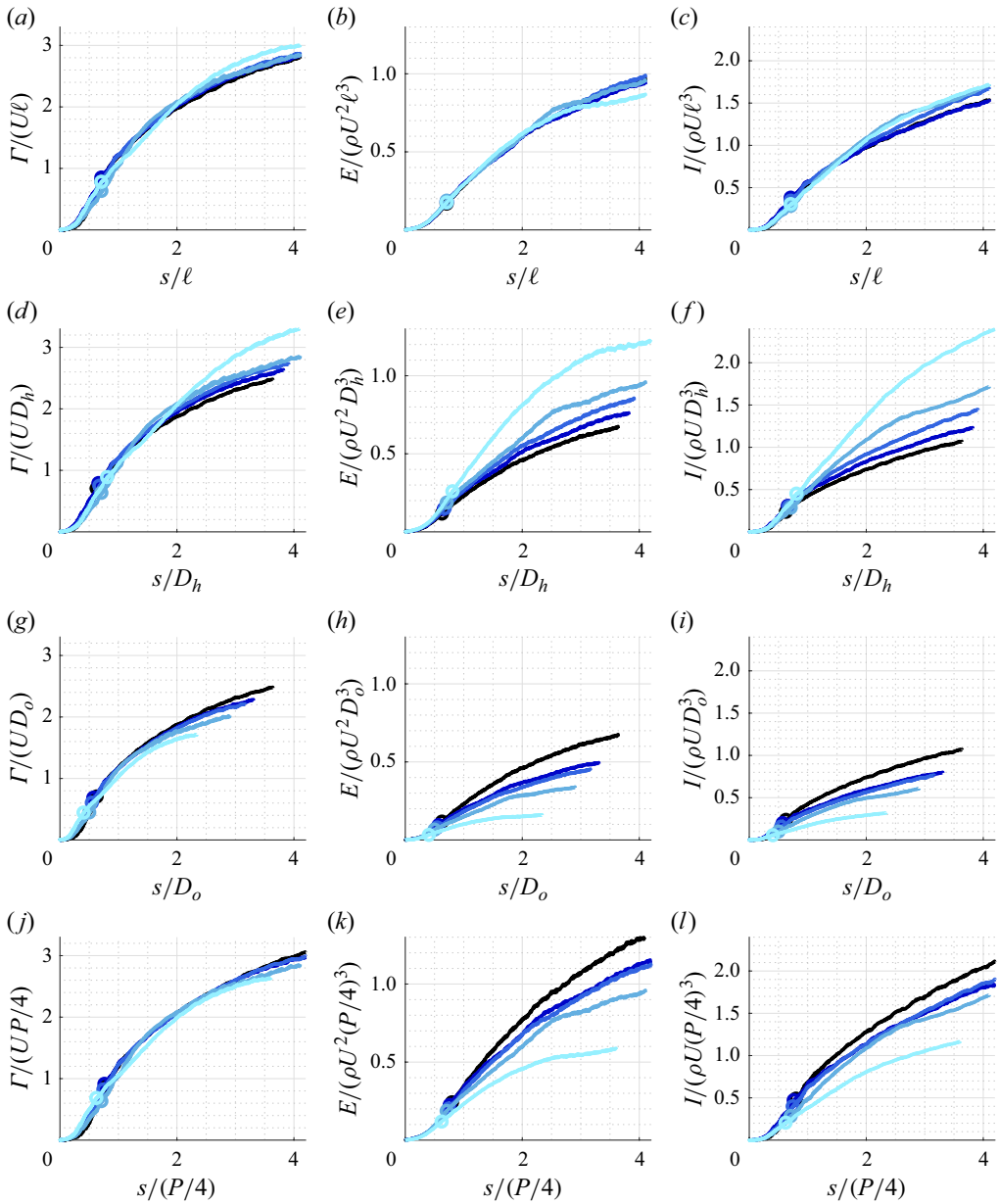


Figure 2. Non-dimensional invariants for all potential scaling factors: triangle (—), square (—), pentagon (—), hexagon (—), circle (—).

## 4. Results and discussion

### 4.1. Scaling of circulation, kinetic energy and hydrodynamic impulse

Non-dimensionalised quantities for the circulation  $\Gamma$ , hydrodynamic impulse  $I$  and kinetic energy  $E$ , as defined in (3.2), are shown in figure 2, as a function of distance travelled  $s$  in the  $x$ -direction. The markers in each plot indicate the location where the plates travel at constant velocity. We first confirm that the non-dimensional circulation behind circular disks, normalised by the hydraulic diameter, is consistent with those found in literature

Length Scale, $L$	$\Gamma$	$E$	$I$	Range ( $s/L$ )
$\ell = \sqrt{A}$	0.031	0.034	0.047	[0, 4.2]
$D_h$	0.062	0.239	0.277	[0, 3.8]
$D_o$	0.067	0.356	0.315	[0, 2.4]
$P/4$	0.045	0.222	0.177	[0, 3.7]

Table 2. The NRMSD for each scaled invariant.

(Yang *et al.* 2012; Fernando & Rival 2016b; de Guyon & Mulleners 2021; Xiang *et al.* 2021). Focusing on figure 2(a,d,g,j), which shows the circulation scaled by the proposed lengths, both  $\ell$  and  $P/4$  collapse  $\Gamma$  well. A clear trend is observed for both the hydraulic diameter and circumscribed diameter: for  $D_h$  the normalised circulation increases as the number of sides on the polygon increases, while the opposite is true for  $D_o$ .

Figure 2(b,e,h,k) shows the kinetic energy. Of all the proposed lengths,  $\ell$  is the only one which appears to collapse the data. There is a small deviation for the triangle plate for  $s > 3\ell$ , which shall be addressed in a later section. As with the circulation, the same trend with the number of edges is observed for the  $D_h$  and  $D_o$  scaling. The perimeter, which appeared to collapse the circulation well, now shows a clear trend, with the normalised energy increasing as the number of sides on the polygon increases.

Finally, figure 2(c,f,i,l) shows the impulse, where we again see that  $\ell$  collapses the data better than the other three proposed lengths. Combined, these results indicate that  $\ell$  is the only length that can scale all three flow invariants.

As a means of quantifying the scaling, the normalised root-mean-squared deviation (NRMSD) of each scaled invariant is provided in table 2. The NRMSD is calculated against the mean of the scaled invariant across all plate geometries, and is normalised by this mean over the observed range. To compare plates on a like-for-like basis, for each scaling parameter  $L$ , scaled invariants were compared only over a range of  $s/L$  in which measurements were available for all plates, as listed in table 2. Consistent with figure 2, table 2 indicates that  $\ell$  is the best scaling parameter for all three invariants. While the NRMSD is similar for all length scales applied to  $\Gamma$ ,  $\ell$  is notably better at scaling  $E$  and  $I$ , approximately six times better for  $E$  and almost four times better for  $I$ .

As mentioned earlier, there is a noticeable deviation in the kinetic energy for the triangle plate for  $s > 3\ell$ . A possible reason for this is that our measurements do not include out-of-plane velocity measurements. Fernando & Rival (2016b) demonstrated that non-axisymmetric plate geometries, such as a square, or an ellipse, are associated with earlier vortex pinch-off and breakdown, which would result in strong out-of-plane velocities. In figure 3, snapshots of the vorticity field behind the circular, triangular and square plates, at non-dimensional distances travelled of  $s/\ell = \{0.5, 1.5, 3.0\}$ , are shown. By  $s = 3\ell$ , a primary vortex behind the triangle plate is not as evident as it is for the other plates, which suggests that the primary vortex has broken down. This, in turn, would lead to more turbulent motion in the wake, which would have higher out-of-plane motions.

#### 4.2. Robustness to flow conditions

While the present experiments were performed for a fixed plate area and acceleration rate, it is worth considering the robustness of the results, and whether they are generalisable to other flow conditions. The present experiment was therefore repeated for the circle, square and triangular plates, having a smaller plate area and a larger acceleration ( $A = 625 \text{ mm}^2$ ,  $\ell = 25 \text{ mm}$ ), which corresponds to a smaller Reynolds number, and faster

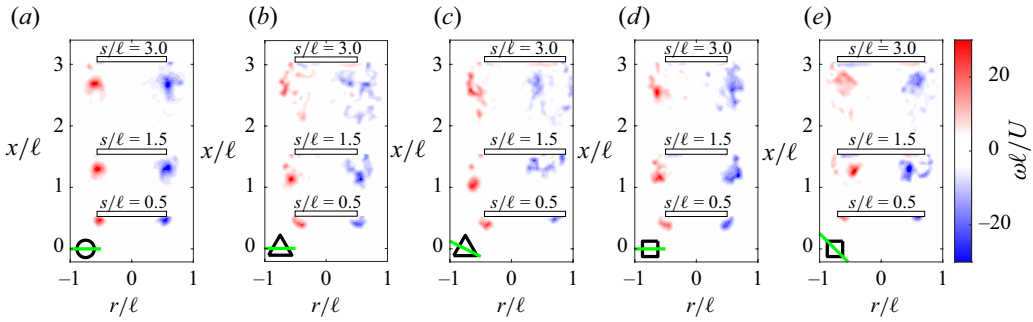


Figure 3. Snapshots of vortex evolution behind (a) circular plate, (b) triangular plate at  $\varphi = 30^\circ$ , (c) triangular plate at  $\varphi = 0^\circ$ , (d) square plate at  $\varphi = 0^\circ$ , (e) square plate at  $\varphi = 45^\circ$ .

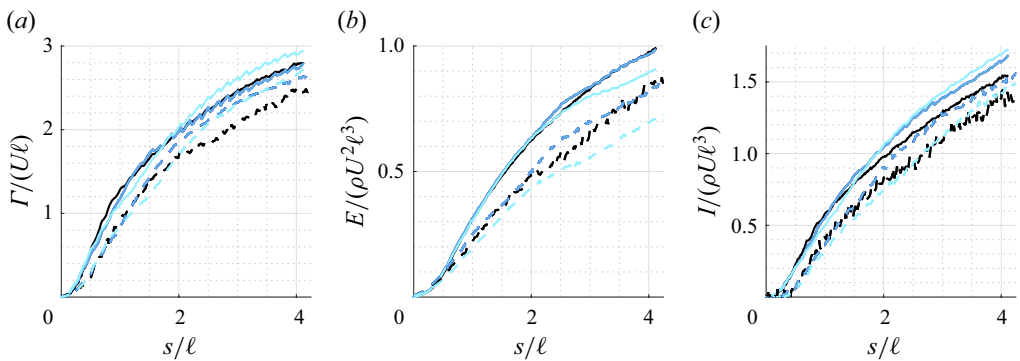


Figure 4. Circulation(a), kinetic energy (b) and hydrodynamic impulse (c) behind triangle (—), square (—), circle (—). Solid lines denote data associated with  $Re = 27\,000$ , while dashed lines denote data associated with  $Re = 19\,000$ .

non-dimensional acceleration ( $Re = 19\,000$ ,  $a^* = 1.33$ ). All other parameters were fixed. Figure 4 shows non-dimensionalised invariants from both sets of experiments. While it is not expected that scaled invariants would collapse across different Reynolds numbers (Fernando & Rival 2016a), figure 4 shows that, with a fixed Reynolds number, the invariants collapse across several plate geometries using  $\ell$ . Note that at a lower Reynolds number, the kinetic energy behind the triangular plate is less than that of the square and circular plates, more noticeably after  $s/\ell \approx 2.5$ .

### 4.3. Considerations of multiple azimuthal planes

Although  $\Gamma$ ,  $E$  and  $I$  are correctly scaled by  $\ell$  for all the plates, it does not imply that their flow fields are identical, as already demonstrated by Higuchi *et al.* (1996) and shown in figure 3. As previously stated, at a given  $s/\ell$  a particular invariant is equal for all plates; however, the vorticity distribution differs from plane to plane. Take, for example, the two planes for the triangle shown in figure 3. Indeed, measuring the circulation, kinetic energy and impulse for the planes shown in figure 3 results in values that are markedly different from those obtained by considering all the measured planes. Relying on a single measurement plane would therefore lead to errors. Prior studies on impulsively started flat plates, however, have typically measured one or two planes at different azimuthal angles. To approximate the circulation of the flow field, Fernando & Rival (2016b) averaged the circulation between the primary and secondary axes of rectangular plates of various

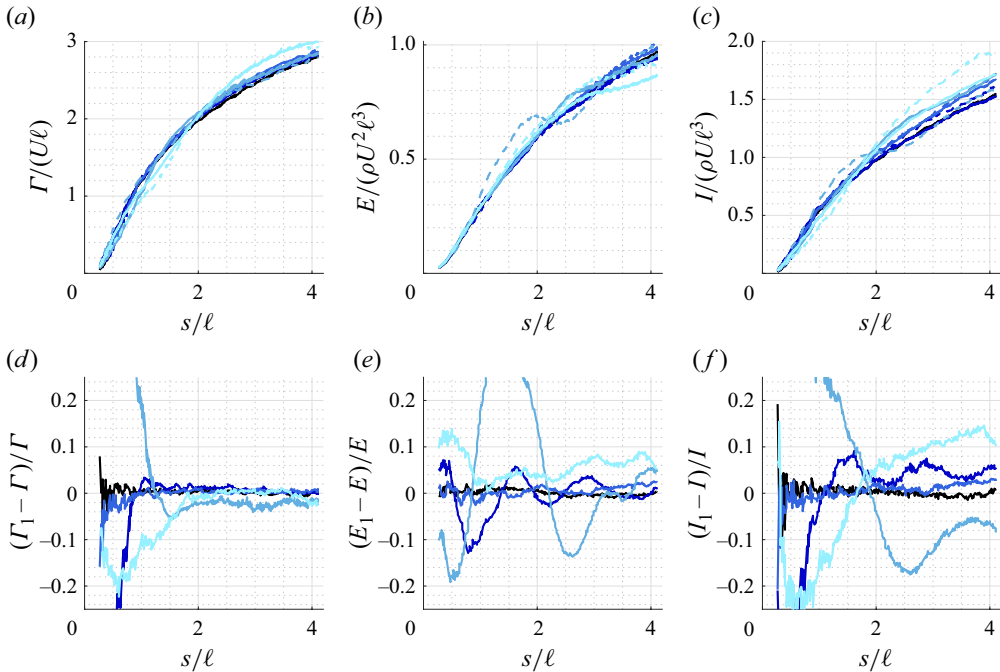


Figure 5. Circulation(a,d), kinetic energy (b,e) and hydrodynamic impulse (c,f) behind triangle (—), square (—), pentagon (—), hexagon (—), circle (—). (a–c) Solid lines represent combined data from all measured axes, dashed lines denote extrapolated data from measurements at a single plane ( $\Gamma_1$ ,  $E_1$ ,  $I_1$ ), aligned with  $\varphi_0$ . (d–f) Relative error of a single measurement plane.

aspect ratios,  $AR$ . For a square plate ( $AR = 1$ ), these planes should have identical flow fields. Kaiser *et al.* (2020), studying plates with a periodic edge, measured two planes, aligned with the peak and trough of the undulating edge, and averaged this information to determine the circulation of the velocity field.

Measurements in as many as 13 azimuthal planes were taken for this study, which allows us to quantify the error in estimating the invariants from a finite number of measurement planes. Figure 5(a–c) shows the calculated invariants from the  $\varphi_0$  plane compared with the invariants from all measurement planes. The error appears negligible for circulation, which would be consistent with Helmholtz’s vortex theorems. For the energy and impulse, however, discrepancies in both the trend and magnitude of both invariants are visible. The relative error is quantified by taking the difference between the measured invariant from a single plane and the value obtained from all measurement planes. The results are presented in figure 5(d–f). For  $s/\ell$ , the relative error for the circulation is generally less than 10%, with the triangle plate producing the largest error and the higher order polygons, including the disk, generally showing negligible error. This error rapidly diminishes to within 4% for  $s > 2\ell$ . No convergence of the error, neither as a function of distance nor plate geometry, is observed for the kinetic energy and impulse, with errors as high as 30% possible.

A similar exercise is repeated for all the measurement planes, and the NRMSD of a one-plane approximation is calculated over  $0 < s/\ell < 4$ . The results are presented in figure 6. For the pentagon, hexagon and disk, measurement of the invariants from any one plane would have an NRMSD error of less than 8%. The square and triangle, however, could have NRMSD as high as 17%, with the lowest error at  $\varphi = 22.5^\circ$  for the square, and approximately  $\varphi = 12.5^\circ$  and  $\varphi = 42.5^\circ$  for the triangle.

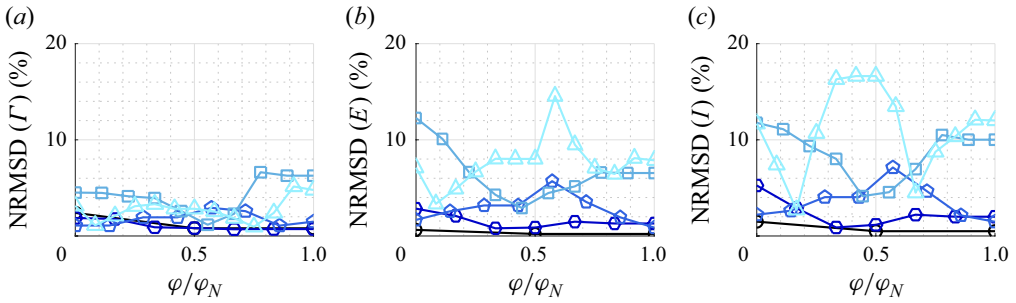


Figure 6. The NRMSD of a single-plane approximation for each invariant: circulation (a), kinetic energy (b) and hydrodynamic impulse (c); triangle ( $\triangle$ ), square ( $\square$ ), pentagon ( $\diamond$ ), hexagon ( $\hexagon$ ), circle ( $\circ$ ).

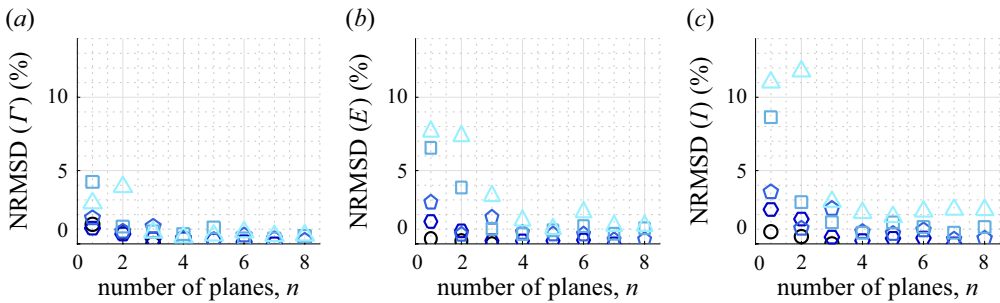


Figure 7. The NRMSD of an  $n$ -plane approximation for each invariant: circulation (a), kinetic energy (b) and hydrodynamic impulse (c); triangle ( $\triangle$ ), square ( $\square$ ), pentagon ( $\diamond$ ), hexagon ( $\hexagon$ ), circle ( $\circ$ ).

Finally, we expand our analysis to consider measurements from  $n$  evenly spaced planes (or the nearest measured plane), between  $\varphi_o$  and  $\varphi_N$ , and calculate the NRMSD of an  $n$ -plane approximation. For  $n = 1$ , the mean results from selecting any individual plane are shown in figure 7. Generally, the error is largest for the triangle and square plate, but the error diminishes as the number of planes increases. For example, behind the square plate, relying on knowledge at  $\varphi_o$  and  $\varphi_N$  individually will produce an NRMSD in  $I$  of 12 %; however, relying on both planes reduces the error to 3 %. For  $n = 3$  equally spaced planes between  $\varphi_o$  and  $\varphi_N$ , the NRMSD is at most 3 % for all invariants.

## 5. Conclusions

The flow behind impulsively started polygonal plates was investigated using PIV. The three invariants of the motions, circulation  $\Gamma$ , hydrodynamic impulse  $I$  and kinetic energy  $E$ , were found to best scale as a function of the square root of the area of the plate  $\ell = \sqrt{A}$ . This length scale performed better at collapsing the invariants compared with the hydraulic diameter, which has typically been used in past studies. This scaling was shown to work at both  $Re = 27\,000$  and  $Re = 19\,000$ , a roughly 40 % change, as well as at two different acceleration rates ( $a^* = 0.785$  and  $a^* = 1.33$ ). Accounting for the three-dimensional topology of the flow is important. Although a single-plane measurement can provide a reasonable approximation for invariants of the motions behind a circular plate, with errors of less than 1 %, the error generally decreases with the number of edges on the polygon plate. Estimating the invariants from a single measurement plane for a square or triangle plate can result in errors as high as 17 %, whereas measurements from three equally spaced planes between  $\varphi_o$  and  $\varphi_N$ , reduce the error to less than 4 %. The current

study limits its scope to regular polygons; however, it would be interesting to extend this work in the future to non-regular geometries, such as rectangles.

**Funding.** This work was supported by funding from the Fonds de Recherche du Québec – Nature et Technologies (FRQNT) no. 287781, and the Natural Sciences and Engineering Research Council (NSERC) no. 698220.

**Declaration of interests.** The authors report no conflict of interest.

#### REFERENCES

- BECKWITH, R.M.H. & BABINSKY, H. 2009 Impulsively started flat plate flow. *J. Aircraft* **46** (6), 2186–2189.
- FAIL, R., LAWFORD, J.A. & EYRE, R.C.W. 1959 Low-speed experiments on the wake characteristics of flat plates normal to an air stream. ARC R & M 3120. Aeronautical Research Council.
- FERNANDO, J.N. & RIVAL, D.E. 2016a Reynolds-number scaling of vortex pinch-off on low-aspect-ratio propulsors. *J. Fluid Mech.* **799**, R3.
- FERNANDO, J.N. & RIVAL, D.E. 2016b On vortex evolution in the wake of axisymmetric and non-axisymmetric low-aspect-ratio accelerating plates. *Phys. Fluids* **28** (1), 017102.
- FERNANDO, J.N., WEYMOUTH, G.D. & RIVAL, D.E. 2020 On the limits of added-mass theory in separated flows and with varying initial conditions. *J. Fluid. Struct.* **93**, 102835.
- GREEN, M.A. & SMITS, A.J. 2008 Effects of three-dimensionality on thrust production by a pitching panel. *J. Fluid Mech.* **615**, 211–220.
- DE GUYON, G. & MULLENERS, K. 2021 Scaling of the translational velocity of vortex rings behind conical objects. *Phys. Rev. Fluids* **6** (2), 024701.
- DE GUYON, G. & MULLENERS, K. 2022 Estimating the non-dimensional energy of vortex rings by modelling their roll-up. *J. Fluid Mech.* **940**, R2.
- HIGUCHI, H., ANDERSON, R.W. & ZHANG, J. 1996 Three-dimensional wake formations behind a family of regular polygonal plates. *AIAA J.* **34** (6), 1138–1145.
- KAISER, F., KRIEGSEIS, J. & RIVAL, D.E. 2020 The influence of edge undulation on vortex formation for low-aspect-ratio propulsors. *J. Fluid Mech.* **883**, A55.
- KUBOTA, Y. & ENDO, Y. 2022 Drag coefficient of a non-convex polygonal plate during free fall. *J. Flow Control Measurement Visualization* **11** (1), 1–13.
- LI, Z., XIANG, Y., QIN, S., LIU, H. & WANG, F. 2022 Two models and the generation mechanisms of the drag on an accelerating starting disk. *Phys. Fluids* **34** (8), 081908.
- LIMBOURG, R. & NEDIĆ, J. 2021 Formation of an orifice-generated vortex ring. *J. Fluid Mech.* **913**, A29.
- NEDIĆ, J., GANAPATHISUBRAMANI, B. & VASSILICOS, J.C. 2013a Drag and near wake characteristics of flat plates normal to the flow with fractal edge geometries. *Fluid Dyn. Res.* **45** (6), 61406.
- NEDIĆ, J., VASSILICOS, J.C. & GANAPATHISUBRAMANI, B. 2013b Axisymmetric turbulent wakes with new nonequilibrium similarity scalings. *Phys. Rev. Lett.* **111** (14), 144503.
- PULLIN, D.I. & WANG, Z.J. 2004 Unsteady forces on an accelerating plate and application to hovering insect flight. *J. Fluid Mech.* **509**, 1–21.
- REIJTENBAGH, J., TUMMERS, M.J. & WESTERWEEL, J. 2023 Drag force on a starting plate scales with the square root of acceleration. *Phys. Rev. Lett.* **130** (17), 174001.
- ROSI, G.A. & RIVAL, D.E. 2017 Entrainment and topology of accelerating shear layers. *J. Fluid Mech.* **811**, 37–50.
- XIANG, Y., LI, Z., QIN, S. & LIU, H. 2021 Formation number and pinch-off signals of disc vortex ring based on a Lagrangian analysis. *Exp. Therm. Fluid Sci.* **129**, 110452.
- YANG, A., JIA, L. & YIN, X. 2012 Formation process of the vortex ring generated by an impulsively started circular disc. *J. Fluid Mech.* **713**, 61–85.